# Mechanochemical Production of Halogen-Bonded Solids Featuring P=O···I−C Motifs and Characterization via X-ray Diffraction, Solid-State Multinuclear Magnetic Resonance, and Density Functional Theory

Yijue Xu, Jasmine Viger-Gravel, Ilia Korobkov, and David L. Bryce*

Department of Chemistry and Biomolecular Sciences & Centre for Catalysis Research and Innovation, University of Ottawa, 10 Marie Curie Private, Ottawa, Ontario K1N 6N5, Canada

S *Supporting Information*

ABSTRACT: A series of phosphine oxide-iodofluorobenzene cocrystals featuring relatively strongly halogen-bonded P=O···I−C motifs has been prepared mechanochemically and characterized by ^{31}P and [17]O solid-state nuclear magnetic resonance (SSNMR) spectroscopy and single-crystal X-ray diffraction. Direct insights were obtained into the correlation between several NMR observables (chemical shift tensors, electric field gradient tensors, and $J(^{31}P, ^{17}O)$ coupling) and the molecular and electronic structure of the halogen bonds. The ^{31}P isotropic chemical shift and span, the [17]O quadrupolar coupling constant and asymmetry parameter, as well as $J(^{31}P, ^{17}O)$ coupling can be strong indicators of the presence of a halogen bond. Density functional theory calculations using periodic boundary conditions have revealed several notable trends. For example, the oxygen isotropic chemical shift and $J(^{31}P, ^{17}O)$ values were found to correlate linearly with the strength of the halogen bond. An additional natural localized molecular orbital (NLMO) investigation shows that the three main contributions to $J(^{31}P, ^{17}O)$ coupling are the P=O bonding orbitals, the oxygen lone pair orbital, and oxygen core orbitals, and that they all together determine the overall trend observed experimentally. Further NLMO analysis revealed a linear correlation between the contribution of the oxygen p_z lone pair orbital to the quadrupolar coupling constant and the strength of the halogen bond. This work, encompassing the first ^{17}O SSNMR studies of halogen bonds, demonstrates how NMR observables provide a useful means to characterize halogen bonds and also improve our understanding of the correlation between the electronic structure of the halogen bond and NMR properties.
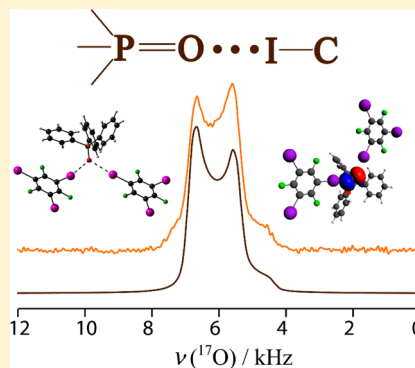
INTRODUCTION

Halogen bonding (XB) is a noncovalent interaction between a region of positive electrostatic potential (σ-hole)[1] of a polarized halogen atom (X = F, Cl, Br, I) and a nucleophilic region of another molecule or functional group.[2,3] The bonding nature of the interaction results in an internuclear distance which is shorter than the sum of the van der Waals radii of the pair of atoms involved in the interaction. Also, since the σ-hole is formed at the outermost pole along the extension of the R−X bond and it is where the halogen bonding interaction occurs,[1] XBs are highly directional, where the R−X···B (R = electron-withdrawing groups and B = Lewis base or anion, etc.) angle tends to be nearly linear.[2] Similar to hydrogen bonds, XB can direct the formation of bifurcated assemblies in the solid state, which has been explored in the design and engineering of supramolecular architectures.[4] Additionally, XB, whose strength ranges from 10 to 200 kJ mol^{-1},[5] is comparable in strength to hydrogen bonding (HB).[6] XB has been receiving an increasing amount of attention in various research fields,[4] e.g., in functional materials (activating efficient phosphorescence),[7] in catalysis (organocatalysts in the Diels−Alder reaction),[8] in biological systems (four-stranded DNA Holliday junction),[6] and in drug design (enhancing

ligand binding by halogenated HIV reverse transcriptase inhibitors).[9]

Solution NMR has played an important role in studying the XB interaction. Recently, Bowling and co-workers studied the effect of solvents on intramolecular XB by ^{13}C, ^{15}N, and ^{19}F solution-state NMR.[10] Ciancaleoni et al. used a combination of NOE NMR and density functional theory (DFT) calculations to roughly quantify the XB/non-XB adducts in solution.[11] However, there is a relative dearth of studies on XB using solid-state NMR. Weingarth et al. reported a measurement of the N···I halogen bond distance by ^{15}N solid-state NMR.[12] Our group is interested in the characterization of noncovalent interactions (i.e., halogen bonds, tetrel bonds, etc.) via SSNMR.[13] This approach provides various advantages which are not available to solution-state NMR, such as eliminating potential interactions with solvent as well as the measurement of complete electric field gradient (EFG) and chemical shift (CS) tensors. From previous investigations in our group, we have demonstrated various

relationships between NMR observables and the XB environments. For example, a series of halogen solid-state NMR experiments and gauge-including projector-augmented wave (GIPAW) DFT calculations showed that the ^{81}Br isotropic chemical shift and span both decrease as the bromide−halogen XB is weakened.[14] An indirect study on cocrystallization of halide salts and *para*-diiodotetrafluorobenzene using ^{13}C NMR showed that the ^{13}C chemical shift increases as the C−I distance increases.[15] Also, multinuclear solid-state magnetic resonance and molecular orbital analysis revealed that halogen quadrupolar coupling constants and asymmetry parameters correlate with the local halogen bonding geometry of type I···X^{-}···I (X = Br or Cl).[16] Most recently, a direct study on halogen-bonded P═Se···I motifs showed an increase in the magnitude of J(^{31}P, ^{77}Se) and ^{77}Se chemical shift values as the XB weakens.[17]

Here, we exploit recent progress in mechanochemistry[18] to prepare and study a series of cocrystals featuring P═O···I−C halogen bonds (Figure 1) using a combination of X-ray
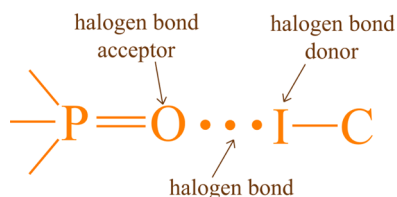
Figure 1. General halogen bonded P═O···I−C moiety.

diffraction (XRD) and solid-state multinuclear magnetic resonance methods. We apply a mechanochemical approach, liquid-assisted grinding (LAG),[19] as an alternative method to synthesize halogen-bonded cocrystals. Since cocrystallization via LAG generates less potentially toxic solvent waste (only a few drops of solvent are needed), it may be more environmentally acceptable than solution crystallization.[20] Also, this method offers an attractive alternative when difficulties are encountered in preparing cocrystals via solution methods. The potential of phosphine oxides as XB acceptors has recently attracted attention. Friščić and co-workers prepared, via LAG, various cocrystals of methyldiphenylphosphine oxide and *para*-diiodotetrafluorobenzene and characterized them with X-ray diffraction.[21] Bowmaker et al. have reported on the mechanochemical preparation of various cocrystals of phosphines and studied them via ^{31}P SSNMR, among other methods.[22] In our study, new halogen-bonded compounds have been prepared through mechanochemical LAG and subsequent slow recrystallization. The geometry of the halogen-bonded compounds has been characterized by single-crystal XRD. ^{31}P cross-polarization magic-angle spinning (CP/MAS) SSNMR spectra are reported, and the ^{31}P chemical shift tensors, which are indirectly characteristic of halogen bonding, are extracted for all halogen-bonded compounds and starting materials.

The ^{17}O isotope is more difficult to observe by NMR spectroscopy due to its electric quadrupole moment (Q = −2.558 fm^2), low natural abundance (0.038%), and extremely low NMR sensitivity relative to ^{1}H (0.0291).[23] Even though the quadrupolar interaction contributes to broad ^{17}O SSNMR line shapes, this method is a proven sensitive tool for probing structure,[24,25] dynamics,[26] and bonding.[25,27,28] Here, we also provide a direct investigation of the relationships between the halogen bonding interaction and the measured NMR parameters for the half-integer spin quadrupolar nucleus ^{17}O (I = 5/2), such as the

quadrupolar coupling constant, C_Q, asymmetry parameter, η_Q, and indirect spin−spin (J) coupling between ^{31}P and ^{17}O, using ^{17}O SSNMR experiments. All of the NMR parameters have also been calculated and interpreted via DFT methods. The computed values are related to the halogen bond strength to help interpret the correlation between the NMR parameters and halogen bonding environment. A further natural localized molecular orbital (NLMO) DFT analysis was conducted to investigate the relationship between the local electronic environment in the presence of a halogen bonding interaction and the observed NMR parameters, J(^{31}P, ^{17}O) and C_Q (^{17}O).

■ EXPERIMENTAL SECTION

Synthesis. *(i). Halogen-Bonded Compounds.* Two halogen bond acceptors (CH$_3$Ph$_2$PO, Ph$_3$PO) and three halogen bond donors (*p*-C$_6$F$_4$I$_2$, *o*-C$_6$F$_4$I$_2$, *sym*-C$_6$F$_3$I$_3$) were purchased from Sigma-Aldrich and used without further purification except for Ph$_3$PO. The purchased Ph$_3$PO, which was a mixture of two polymorphs (monoclinic and orthorhombic), was recrystallized from acetone to give the monoclinic polymorph before use in further reactions. The preparations of two halogen-bonded compounds containing *p*-C$_6$F$_4$I$_2$ were performed using a procedure adapted from the literature.[21,29] Halogen-bonded compounds were produced by LAG, whereby equimolar amounts of starting material were ground in a mortar and pestle with a trace amount of acetonitrile for about 20 min.[30] The amounts of starting materials used for synthesis are listed in Table S1 in the Supporting Information. The mixture was subsequently dissolved in a small vial containing a minimum amount of acetonitrile and slowly evaporated at room temperature until the products crystallized, yielding the halogen-bonded compounds: (Ph$_3$PO)(*p*-C$_6$F$_4$I$_2$)$_2$ (**A1**), (Ph$_3$PO)(*o*-C$_6$F$_4$I$_2$)$_2$ (**A2**), (Ph$_3$PO)(*sym*-C$_6$F$_3$I$_3$) (**A3**), (CH$_3$Ph$_2$PO)(*p*-C$_6$F$_4$I$_2$) (CH$_3$CN) (**B1**), and (CH$_3$Ph$_2$PO)(*sym*-C$_6$F$_3$I$_3$)$_2$ (**B3**). Comparison between PXRD and solid-state NMR data acquired before and after recrystallization from slow evaporation (Figure S3 in the Supporting Information) confirmed that the halogen-bonded cocrystals were produced by LAG.

(ii). ^{17}O-Labeled Halogen-Bonded Compounds. The synthesis of ^{17}O-labeled Ph$_3$PO was carried out as described in literature.[31] An amount of 1.5 g of Ph$_3$P was dissolved in 20 mL dry dichloromethane in an ice bath under argon. An amount of 0.3 mL of bromine dissolved in another 20 mL of dry dichloromethane was added dropwise to the previous solution under continuous cooling. After the solution was allowed to warm to room temperature, 0.1 mL of 40% ^{17}O-enriched H$_2$O was added and stirred overnight, which formed a separate water phase at first but disappeared later to give a clear dark orange solution. The solution was washed three times with 10% Na$_2$CO$_3$ solution, which yielded a light yellow product but turned colorless eventually. Finally, the solution was dried with MgSO$_4$. An amount of 1.1080 g (70% yield) of monoclinic Ph$_3$P^{17}O was obtained after recrystallization from acetone. ^{17}O-labeled halogen-bonded compounds were synthesized as described above, using Ph$_3$P^{17}O as starting material.

Single-Crystal X-ray Crystallography. Data collection results for compounds **A1**, **A2**, **A3**, **B1**, and **B3** represent the best data sets obtained in several trials for each sample. The crystals were mounted on thin glass fibers using paraffin oil. Prior to data collection, crystals were cooled to 200.15 K. Data were collected on a Bruker AXS SMART single-crystal diffractometer equipped with a sealed Mo tube source (wavelength 0.71073 Å) APEX II CCD detector. Raw data collection and processing were performed

with the APEX II software package from BRUKER AXS.[32] Diffraction data for **B1**, **A1**, and **B3** samples were collected with a sequence of 0.3° ω scans at 0, 120, and 240° in φ. Due to lower unit cell symmetry, in order to ensure adequate data redundancy, diffraction data for **A2** and **A3** were collected with a sequence of 0.3° ω scans at 0, 90, 180, and 270° in φ. Initial unit cell parameters were determined from 60 data frames with 0.3° ω scan each, collected at the different sections of the Ewald sphere. Semiempirical absorption corrections based on equivalent reflections were applied.[33] Systematic absences in the diffraction data set and unit cell parameters were consistent with triclinic $P\bar{1}$ (No. 2) for compounds **A2** and **A3**, monoclinic $P2_1/c$ (No. 14) for compound **A1**, monoclinic $P2_1/n$ (No. 14, alternative settings) for compound **B3**, and orthorhombic $Pnma$ (No. 62) for **B1**. Solutions in the centrosymmetric space groups for all reported compounds yielded chemically reasonable and computationally stable results of refinement. The structures were solved by direct methods, completed with difference Fourier synthesis, and refined with full-matrix least-squares procedures based on F^2.

For all compounds, all hydrogen atomic positions were calculated based on the geometry of related non-hydrogen atoms and constrained to the riding model. All hydrogen atoms were treated as idealized contributions during the refinement. All scattering factors are contained in several versions of the SHELXTL program library, with the latest version used being v.6.12.[34] Further information on the structure refinements is given in the Supporting Information.

Powder X-ray Diffraction. Sample phase purity was verified by X-ray powder diffraction analysis (shown in Figure S1 and S2 in the Supporting Information) using a Rigaku Ultima IV diffractometer at room temperature (298 ± 1 K) with a copper source and one diffracted beam monochromator and with 2θ ranging from 5° to 50° in increments of 0.02° at a rate of 1° per minute. Simulations were generated using Mercury 3.6 software from the Crystallographic Data Center.

Solid-State NMR Spectroscopy. Bruker consoles were used to acquire data at the University of Ottawa using 4.7, 9.4, and 11.7 T magnets and at the National Ultrahigh-field NMR Facility for Solids in Ottawa using a 21.1 T magnet. A 7 mm Bruker HXY MAS probe was employed for experiments at 4.7 T. Experiments at 9.4 and 11.7 T used a 4 mm Bruker HXY probe or 7 mm Bruker HXY MAS probe, while experiments at 21.1 T used a 4 mm Bruker HX MAS probe and a home-built solenoid 5 mm HX static probe (PM#7).

(i). ^{31}P SSNMR. The ^{31}P SSNMR spectra of all halogen-bonded compounds were acquired at 4.7 T ($\nu_L(^{31}\text{P}) = 80.997$ MHz) and at 9.4 T ($\nu_L(^{31}\text{P}) = 161.976$ MHz). The chemical shifts were referenced to ammonium dihydrogen phosphate ($\delta_{iso} = 0.81$ ppm with respect to H_3PO_4 in 85% D_2O). The MAS frequency was varied from 6 to 2.5 kHz to obtain spectra with a sufficient number of sidebands for spectral fitting purposes. A standard cross-polarization pulse sequence was employed. The $\pi/2$ pulse length and contact time were 3.6 μs and 1.5 ms, respectively. The relaxation delay varied from 50 to 120 s for Ph_3PO compounds and from 2 to 15 s for CH_3Ph_2PO compounds. Compound **B2** is a noncrystalline solid and has a low decomposition point (39 °C). Only one phase cycle (^{31}P CP/MAS) was acquired for this compound at 4.7 T before the sample decomposed, as assessed in a second experiment with a larger number of scans.

(ii). ^{17}O SSNMR. The ^{17}O chemical shifts were referenced to liquid water ($\delta_{iso} = 0.00$ ppm). Synthesized ^{17}O-Ph_3PO was

packed into a 7 mm o.d. zirconia rotor, and halogen-bonded compounds were packed into separate 4 mm o.d. zirconia rotors. The ^{17}O SSNMR spectra of all halogen-bonded compounds were acquired at 9.4 T ($\nu_L(^{17}\text{O}) = 54.250$ MHz), 11.7 T ($\nu_L(^{17}\text{O}) = 67.800$ MHz), and also 21.1 T ($\nu_L(^{17}\text{O}) = 121.984$ MHz).

9.4 T. ^{17}O MAS and stationary solid-state NMR spectra of ^{17}O-labeled Ph_3PO were obtained at 9.4 T using a 7 mm triple resonance MAS probe. A Hahn-echo experiment (i.e., $\pi/2 - \tau_1 - \pi - \tau_2 - $acq) with TPPM proton decoupling was employed. The $\pi/2$ pulse length was 7.5 μs. The CT (central transition) selective pulse length was 2.5 μs, and the interpulse delay was 6 μs. A relaxation delay of 4 s was used to acquire 30 720 scans for static spectra and 15 456 scans for MAS spectra. The MAS rate was 6.5 kHz.

11.7 T. A solid echo (i.e., $\pi/2 - \tau_1 - \pi/2 - \tau_2 - $acq) pulse sequence with CW proton decoupling was applied for the solid-state ^{17}O MAS experiments at a spinning rate of 10 kHz using a 4 mm low γ double resonance MAS probe with a relaxation delay of 10 s for **A1** and **A3** and 5 s for **A2**. The $\pi/2$ pulse length was 3.9 μs, while the echo delay was 98.7 μs. The CT selective pulse length was 1.3 μs, and 20k to 30k scans were required.

21.1 T. A one-pulse sequence without proton decoupling was applied for the solid-state MAS NMR experiments at a spinning rate of 10 kHz along with a relaxation delay of 5 s for all of the ^{17}O-labeled halogen-bonded samples. The $\pi/2$ pulse length was 9 μs. The CT selective pulse length was 3 μs. 6144 scans were acquired. Static ^{17}O NMR spectra were acquired using a solid echo (i.e., $\pi/2 - \tau_1 - \pi/2 - \tau_2 - $acq) pulse sequence with CW proton decoupling. The echo delay was 50 μs. A relaxation delay of 5 s was used to acquire 10k scans.

Spectra were simulated using the Herzfeld−Berger analysis (HBA)[35] and WSolids[36] programs.

Quantum Chemical Calculations. The ^{31}P and ^{17}O magnetic shielding tensors and ^{17}O EFG tensors were calculated with Materials Studio and CASTEP[37] software version 4.4 using periodic boundary conditions and the GIPAW DFT method, and in a second instance with Amsterdam Density Functional (ADF) software[38] using cluster models.

The input file generated from Materials Studio used "on-the-fly" pseudopotentials to perform the geometry optimization of the hydrogen positions. The energy cut-offs and k-point grids used are shown in Table S2 in the Supporting Information. The GIPAW DFT calculations were applied to calculate all the NMR parameters.[39]

Cluster models were generated using the X-ray crystal structures' atomic coordinates. The ADF calculation was carried out using the High Performance Computing Virtual Laboratory (HPCVL). First, optimization of the hydrogen positions was done at the TPSS/6-311++G** level using Gaussian 09[40] before the NMR calculation. Calculations of $J(^{31}\text{P}, ^{17}\text{O})$ were performed using ADF with scalar relativistic effects via the zeroth-order regular approximation (ZORA). The meta-GGA TPSS functional was used with the ZORA/DZP basis set. Magnetic shielding and EFG tensors were also determined using ADF but with the revPBE functional and the ZORA/TZP basis set including scalar relativistic effects. NLMO analyses were further carried out to calculate all contributions to the J coupling tensors and EFG tensors, and the orbitals were visualized with the program adfview.

The magnetic shielding tensors (σ in ppm) were converted to CS tensors (δ in ppm) using the following equation: $\delta_{ij} = ((\sigma_{ref} - \sigma_{ij})/(1 - \sigma_{ref}))$ (where $\sigma_{ref} = 331.51$ for phosphorus, δ_{ij} is
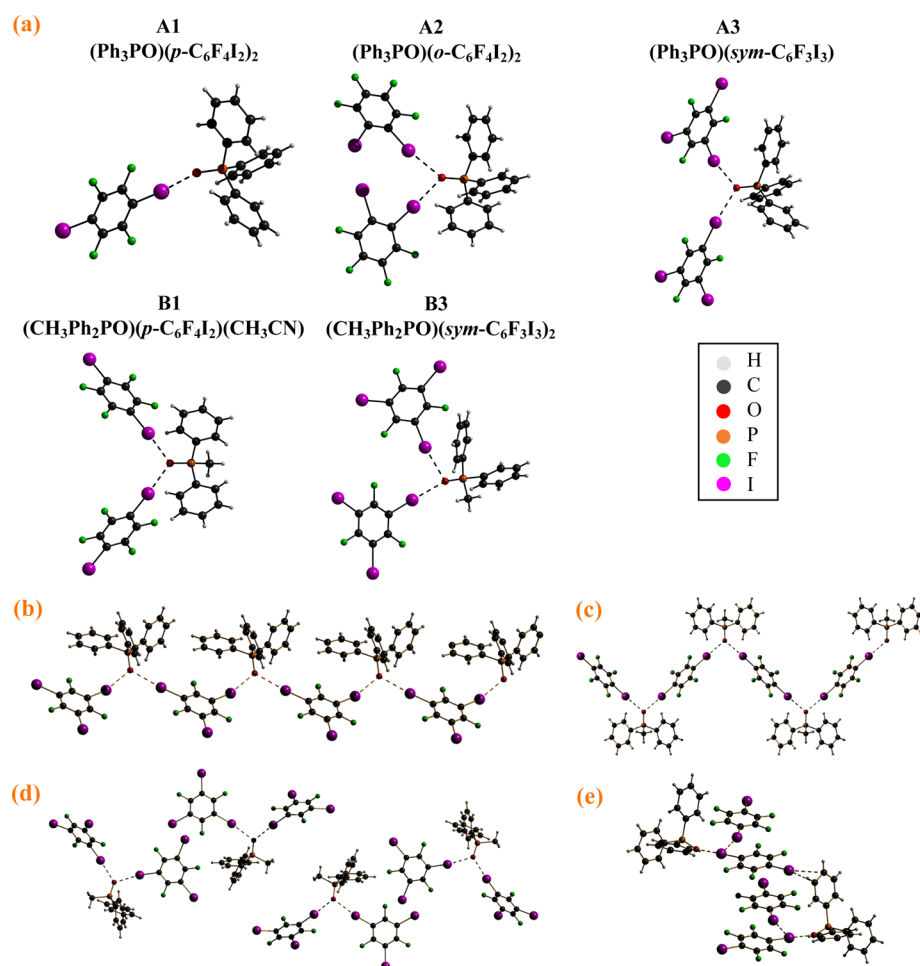
Figure 2. (a) Intermolecular geometries for halogen-bonded compounds **A1**, **A2**, **A3**, **B1**, and **B3** from single-crystal X-ray diffraction. The crystal structure of **A2** shows 2-fold disorder of one of the aromatic rings. Atom colors: iodine is violet; fluorine is green; oxygen is red; phosphorus is orange; carbon is black; and hydrogen is white. (b) Zigzag fragment of the halogen-bonded framework in compound **A3**. (c) Zigzag fragment of the halogen-bonded framework in compound **B1**. (d) Discrete halogen-bonded entities in compound **B3**. (e) Fragment of the cocrystal structure of **A1**, displaying short I···I and I···C contacts.

the chemical shift tensor component, and σ_{ij} is the magnetic shielding tensor component).[41] The absolute chemical shift scale for oxygen,[42] $\sigma_{\mathrm{ref}} = 287.5$ ppm, was employed to convert the ^{17}O magnetic shielding tensors to chemical shifts.

■ RESULTS AND DISCUSSION

X-ray Crystal Structures. Although the LAG method inherently does not generally allow one to characterize the products by single-crystal XRD, and one may be left with unreacted starting materials, this mechanochemical method is still attractive due to its ability to increase the yield of reaction and efficiency when the solubility of the compounds is limited.[30] With high efficiency and yield in mind, we have used LAG as a synthetic and screening method to discover a series of halogen-bonded compounds, $(\mathrm{Ph_3PO})(o\text{-}\mathrm{C_6F_4I_2})_2$ (**A2**), $(\mathrm{Ph_3PO})(sym\text{-}\mathrm{C_6F_3I_3})$ (**A3**), $(\mathrm{Ch_3Ph_2PO})(sym\text{-}\mathrm{C_6F_3I_3})_2$ (**B3**), $(\mathrm{Ph_3PO})(p\text{-}\mathrm{C_6F_4I_2})_2$ (**A1**), and $(\mathrm{CH_3Ph_2PO})(p\text{-}\mathrm{C_6F_4I_2})$ $(\mathrm{CH_3CN})$ (**B1**). For characterization by single-crystal XRD, samples were recrystallized. The consistency between the cocrystals obtained first by LAG and then by subsequent slow evaporation was verified by powder X-ray diffraction (see Supporting Information).

The local halogen bonding environments as determined by single-crystal XRD are shown in Figure 2(a) for **A1**, **A2**, **A3**, **B1**,

and **B3**. The structures of **A1** and **B1** represent previously unidentified crystalline compounds which do not correspond to similar previously reported systems.[21,29] $(\mathrm{CH_3Ph_2PO})(o\text{-}\mathrm{C_6F_4I_2})$ (**B2**) is a noncrystalline solid (no crystal structure is accessible). We report several selected intermolecular contact distances and angles in Table 1 that are used to characterize the halogen bonding interaction and geometry, which include the halogen bond length, $d_{\mathrm{I\cdots O}}$, the carbon–iodine bond length, $d_{\mathrm{I-C}}$, the phosphorus–oxygen bond length, $d_{\mathrm{P=O}}$, O···I–C angle, $\theta_{\mathrm{O\cdots I-C}}$, P=O···I angle, $\theta_{\mathrm{P=O\cdots I}}$, and I···O···I angle, $\theta_{\mathrm{I\cdots O\cdots I}}$. R_{XB}, a normalized distance parameter, represents the ratio of the short contact distance between the halogen bond donor (i.e., I) and halogen bond acceptor (i.e., O) to the sum of their van der Waals radii (1.52 Å for O and 1.98 Å for I)[43]

$$R_{\mathrm{XB}} = \frac{d_{\mathrm{I\cdots O}}}{\sum d_{\mathrm{vdW}}}$$

It is a qualitative measurement of the halogen bond strength. The crystallographic data for all compounds are given in Table 2, and full cif files are available as Supporting Information.

A polymorph of **A1** has been described previously as a zigzag halogen-bonded chain since oxygen acts as a bifurcated halogen bond acceptor.[29] Here, we report another $P2_1/c$ monoclinic

Table 1. Local Halogen Bonding Geometrical Information from Single-Crystal X-ray Diffraction

	compound	#I	$d_{I\cdots O}$/Å	d_{I-C}/Å	$d_{P=O}$/Å	R_{XB} [a]	$\theta_{O\cdots I-C}$/°	$\theta_{P=O\cdots I}$/°	$\theta_{I\cdots O\cdots I}$/°	R_{DD} [b]/Hz
A1 [c]	$(Ph_3PO)(p\text{-}C_6F_4I_2)_2$	1	2.725	2.092	1.495	0.779	175.7	152.1	n.a.	−1975
A2	$(Ph_3PO)(o\text{-}C_6F_4I_2)_2$	1	2.896	2.095	1.498	0.827	176.8	132.9	92.4	−1964
		2	2.888	2.106		0.825	169.4	132.0		
A3	$(Ph_3PO)(sym\text{-}C_6F_3I_3)$	1	2.920	2.091	1.491	0.834	174.5	127.0	107.0	−1991
		2	2.979	2.081		0.851	163.8	116.4		
B1 [d]	$(CH_3Ph_2PO)(p\text{-}C_6F_4I_2)(CH_3CN)$	1	2.847	2.089	1.500	0.813	175.7	130.4	90.4	−1956
B3	$(CH_3Ph_2PO)(sym\text{-}C_6F_3I_3)_2$	1	2.915	2.083	1.497	0.833	171.0	118.2	95.3	−1968
		2	2.826	2.097		0.808	176.1	123.9		

[a] R_{XB} is the normalized distance parameter, $R_{XB} = d_{I\cdots O}/\sum d_{vdW}$, where $d_{I\cdots O}$ is the shortest distance between the oxygen and iodine and $\sum d_{vdW}$ is the sum of their van der Waals radii (1.52 Å for O and 1.98 Å for I). [b] ^{31}P,^{17}O direct dipolar coupling constant, $R_{DD} = (\mu_0/(4\pi))(\hbar/(2\pi))\gamma_P\gamma_O \langle r_{PO}^{-3}\rangle$, where γ_P and γ_O are the magnetogyric ratios for ^{31}P and ^{17}O, respectively and $\langle r_{PO}^{-3}\rangle$ is the motionally averaged inverse cube of the phosphorus−oxygen internuclear distance. [c] Contains one extra $p\text{-}C_6F_4I_2$, which is not involved in halogen bonding. [d] This compound is a solvate (acetonitrile).

Table 2. Crystallographic Data and Selected Data Collection Parameters for Halogen-Bonded Compounds

	A1	A2	A3	B1	B3
empirical formula	$C_{30}H_{15}F_8I_4OP$	$C_{30}H_{15}F_8I_4OP$	$C_{24}H_{15}F_3I_3OP$	$C_{21}H_{16}F_4I_2NOP$	$C_{25}H_{13}F_6I_6OP$
formula wt.	1081.99	1081.99	788.03	659.12	1235.72
cryst size, mm^3	$0.290 \times 0.220 \times 0.160$	$0.260 \times 0.070 \times 0.050$	$0.220 \times 0.220 \times 0.160$	$0.360 \times 0.260 \times 0.230$	$0.230 \times 0.210 \times 0.180$
cryst system	monoclinic	triclinic	triclinic	orthorhombic	monoclinic
space group	$P2_1/c$	$P\bar{1}$	$P\bar{1}$	$Pnma$	$P2_1/n$
Z	4	2	2	4	4
a, Å	9.3190(6)	8.6823(2)	9.7436(2)	21.9816(16)	8.4758(3)
b, Å	25.4268(18)	12.8395(2)	10.7585(2)	18.0739(14)	44.7106(15)
c, Å	13.8063(9)	15.1270(3)	13.5453(3)	5.8075(4)	9.2023(3)
α, deg	90	90.4885(10)	113.1738(10)	90	90
β, deg	103.9422(17)	97.5416(10)	96.9048(10)	90	115.9700(15)
γ, deg	90	105.8860(11)	107.4200(11)	90	90
volume, Å^3	3175.1 (4)	1606.12(6)	1198.74(4)	2307.3(3)	3135.15(19)
calculated density, Mg m^{-3}	2.264	2.237	2.183	1.897	2.618

crystal system in which oxygen acts as a single halogen bond acceptor with a near linear angle of 175.7° and which forms a discrete 1:1 entity through interaction with the iodine atom in $p\text{-}C_6F_4I_2$. It has a low R_{XB} value, 0.779 (the smallest in the present study), which implies a strong halogen bond. As shown in Figure 2(e), the other iodine atom in the same $p\text{-}C_6F_4I_2$ molecule interacts with a phenyl ring in Ph_3PO with I···C distances of 3.426 and 3.378 Å. Another crystallographically distinct $p\text{-}C_6F_4I_2$ molecule has a weak I···I interaction with the first $p\text{-}C_6F_4I_2$ with a distance of 3.854 Å.

Compound **A2** packs in the triclinic crystal system and $P\bar{1}$ space group and features 2-fold disorder of one of the $o\text{-}C_6F_4I_2$ molecules. One of the two orientations is depicted in Figure 2(a); both orientations and full crystallographic information are given in the Supporting Information. Two halogen bond donors with iodine atoms facing each other interact with one oxygen atom with an I···O···I angle of 92.4°. One of the iodines interacts with oxygen with a near linear O···I−C angle of 176.8° and R_{XB} value of 0.827. The O···I−C angle for the second $o\text{-}C_6F_4I_2$ moiety is 169.4°, and the R_{XB} value is 0.825.

Compound **A3** packs in the triclinic crystal system and $P\bar{1}$ space group. The oxygen acts as a bifurcated halogen bond acceptor, interacting with two iodines with O···I−C angles of 174.5° and 163.8°, providing a zigzag chain (Figure 2(b)). The I···O···I angle is 107°. The halogen bonds are moderately strong, as characterized by R_{XB} values of 0.834 and 0.851.

The crystal structure of **B1**, which is orthorhombic, shows a crystallographic symmetry between two $p\text{-}C_6F_4I_2$ molecules, with a bifurcated I···O···I angle of 90.4°, which is different from that

observed for a different polymorph.[21] The O···I−C angle is 175.7°, and the R_{XB} value is 0.813. Acetonitrile molecules crystallize in the unit cell. Instead of acting as a single halogen bond acceptor, the oxygen interacts with two iodine atoms with the same angle and the same distance yielding a bidentate acceptor, thus forming a polymeric zigzag chain and providing a one-dimensional network (Figure 2(c)). We were unfortunately unable to obtain an X-ray powder pattern which matched this crystal structure (shown in Figure S1), which suggests that grinding or recrystallization has an influence on the structure.

B3 crystallizes in the $P2_1/n$ monoclinic space group. The oxygen atom again halogen bonds with two iodine atoms, forming a I···O···I angle of 95.3°. The R_{XB} values are 0.833 and 0.808. The two O···I−C angles are 171° and 176.1°. However, unlike the crystal structure of **A3**, in which other iodines can form additional halogen bonding interactions to create a zigzag chain, the structure of **B3** shows of only one halogen bonding interaction for each $sym\text{-}C_6F_3I_3$. As a result, discrete halogen-bonded entities, as opposed to the zigzag chains found in **A3**, are observed for **B3** (shown in Figure 2(d)).

Solid-State NMR Spectroscopy. (i). ^{31}P CP/MAS NMR. Since ^{16}O is NMR-silent and ^{127}I has a large quadrupole moment (Q) leading to broad resonances, we first focus on a solid-state NMR study of ^{31}P ($I = 1/2$; natural abundance of 100%), which is indirectly involved in the halogen bonding interaction, to probe the halogen bond acceptor moieties (see a general P=O···I−C moiety in Figure 1).

The ^{31}P CP/MAS SSNMR spectra of the starting materials, Ph_3PO and CH_3Ph_2PO, and their respective halogen-bonded
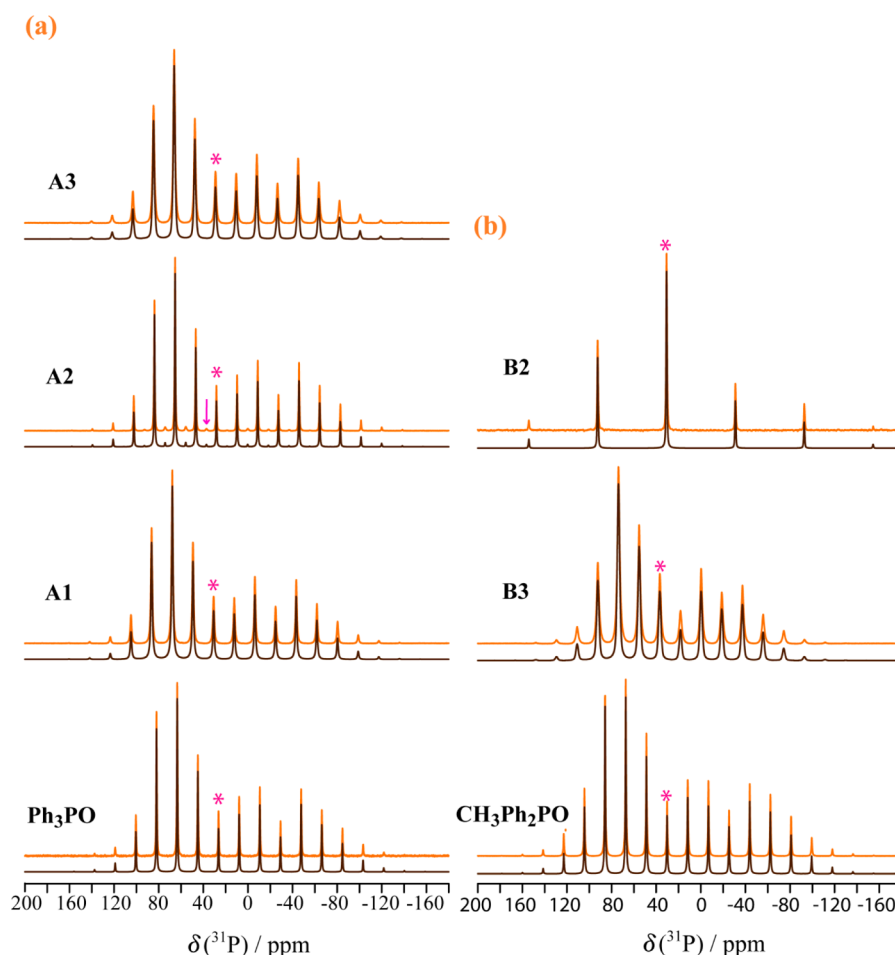
Figure 3. Experimental ^{31}P CP/MAS SSNMR spectra (orange) obtained at 9.4 T for (a) monoclinic Ph$_3$PO and its halogen-bonded compounds (**A1**, **A2**, **A3**) and (b) CH$_3$Ph$_2$PO and its halogen-bonded compound (**B3**). The corresponding simulated spectra are shown at the bottom (brown). The isotropic peaks are indicated by pink asterisks. The spectra were acquired at a spinning speed of 3 kHz to obtain a good number of spinning sidebands. The ^{31}P center band of a small impurity in compound **A2** is shown with a pink arrow. The spectrum for **B2** was obtained at 4.7 T, and the spinning speed was 5 kHz.

Table 3. Experimental ^{31}P Chemical Shift Tensors and $J(^{31}$P, ^{17}O) Values^e

|	compound	δ_{iso}/ppm^a	Ω/ppm^a	κ^a	$J_{iso}(^{31}$P, ^{17}O)/Hz	R_{eff}/Hz^b	ΔJ/Hz^f
	monoclinic Ph$_3$PO^c	26.3 (0.3)	198 (7)	0.87 (0.01)	160 (4)	−1800 (50)	−650 (150)
A1	(Ph$_3$PO)(p-C$_6$F$_4$I$_2$)$_2$	30.7 (0.2)	183 (4)	0.98 (0.06)	157 (5)	−1800 (100)	−790 (300)
A2^d	(Ph$_3$PO)(o-C$_6$F$_4$I$_2$)$_2$	28.3 (0.2)	193 (2)	0.88 (0.01)	154 (4)	−1800 (100)	−570 (300)
A3	(Ph$_3$PO)(sym-C$_6$F$_3$I$_3$)	29.1 (0.1)	190 (4)	0.84 (0.08)	155 (4)	−1700 (200)	−800 (600)
	CH$_3$Ph$_2$PO	30.2 (0.1)	216 (4)	0.69 (0.02)	---	---	---
B2	(CH$_3$Ph$_2$PO)(o-C$_6$F$_4$I$_2$)	30.7 (0.1)	215 (4)	0.70 (0.03)	---	---	---
B3	(CH$_3$Ph$_2$PO)(sym-C$_6$F$_3$I$_3$)$_2$[31]	36.7 (0.1)	171 (2)	0.84 (0.03)	---	---	---

^{a}Isotropic chemical shift: $\delta_{iso} = (\delta_{11} + \delta_{22} + \delta_{33})/3$, span: $= \delta_{11} - \delta_{33}$, skew: $\kappa = 3(\delta_{22} - \delta_{iso}/\Omega$, where $\delta_{11} \geq \delta_{22} \geq \delta_{33}$. $^bR_{eff}$ is the effective dipolar coupling constant and is defined as $R_{eff} = R_{DD} - \Delta J/3$, where ΔJ is the anisotropy in J. ^{c}CS tensors have also been previously reported by Arumugam et al.,[44] and $J(^{31}$P, ^{17}O) has been previously reported by Bryce et al.[31] ^{d}**A2** contains a trace impurity (δ_{iso} = 37.2(0.2) ppm, Ω = 143(15) ppm, κ = 0.84(0.17)). ^{e}Error bounds are in brackets. ^{f}Errors in ΔJ are calculated from errors in R_{eff}.

compounds, are shown in Figure 3. The CS tensor parameters (isotropic chemical shift (δ_{iso}), span (Ω), and skew (κ)) are reported in Table 3. Spinning the sample at different MAS frequencies helps to differentiate the isotropic peaks from the spinning sidebands and provides improved precision in the fitted parameters (^{31}P CP/MAS SSNMR spectra acquired at 4.7 T with different spinning speeds are provided in Figure S6 in the Supporting Information). The purchased Ph$_3$PO is a mixture of two polymorphs, monoclinic (δ_{iso} = 26.3 ppm) and orthorhombic

(δ_{iso} = 28.1 ppm) (see relevant ^{31}P NMR spectra in Figure S5 in the Supporting Information), consistent with previous work by Arumugam and co-workers.[44] Further recrystallization from acetone generated pure monoclinic Ph$_3$PO.

The halogen-bonded compounds **A1**, **A2**, and **A3** have larger ^{31}P isotropic chemical shifts and marginally smaller ^{31}P CS tensor spans compared to starting material monoclinic Ph$_3$PO (δ_{iso} = 26.3 ppm, Ω = 198 ppm). The same holds when comparing halogen-bonded compounds **B2** and **B3** to CH$_3$Ph$_2$PO
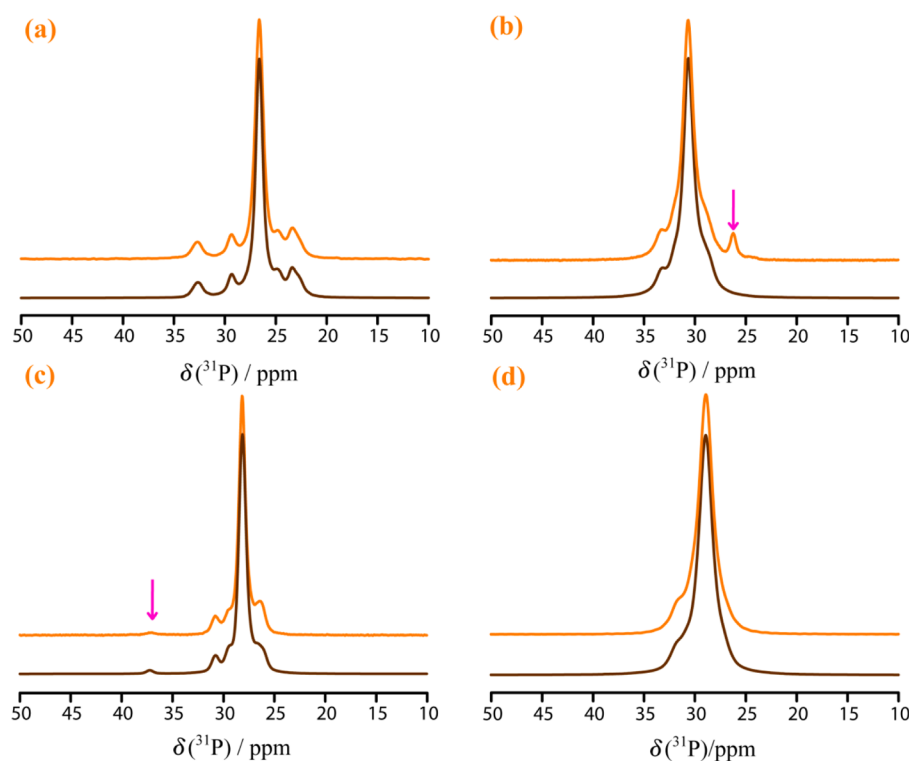
Figure 4. Experimental ^{31}P CP/MAS SSNMR spectra (orange) obtained at 4.7 T for (a) Ph_3PO and 9.4 T for its halogen-bonded compounds (b) **A1**, (c) **A2**, and (d) **A3**. The corresponding simulated spectra are shown at the bottom (brown). The MAS speed varies from 4 to 5 kHz. Impurities in **A1** and **A2** are shown with pink arrows.

(δ_{iso} = 30.2 ppm, Ω = 216 ppm). Although the spectral differences are small, this is perhaps unsurprising given that ^{31}P is an indirect probe of the O···I interaction, one bond removed. The trend observed here for $\delta_{iso}(^{31}P)$ mirrors that for $\delta_{iso}(^{13}C)$ of the *ipso* carbon atoms in a series of halogen-bonded diiodotetrafluorobenzene complexes.[15] Taken together, the values of δ_{iso}, Ω, and κ reported for ^{31}P in Table 3 are sensitive enough to distinguish between all of the halogen-bonded and nonhalogen-bonded compounds in this study.

(ii). ^{31}P and ^{17}O SSNMR Spectroscopy of Halogen-Bonded Cocrystals of ^{17}O-Labeled Ph_3PO. The monoclinic ^{17}O-enriched Ph_3PO from the corresponding phosphine was prepared according to the literature.[31] $Ph_3P^{17}O$ was used as the starting material to further synthesize ^{17}O-labeled halogen-bonded compounds. ^{17}O EFG and CS tensors are expected to provide new insights into the nature of the halogen-bonded P=O···I−C motif.

The ^{31}P CP/MAS NMR spectrum of monoclinic ^{17}O-labeled Ph_3PO, acquired at 4.7 T, is shown in Figure 4(a). The ^{31}P CS tensor magnitudes and $J_{iso}(^{31}P, ^{17}O)$ can be extracted by fitting the ^{31}P CP/MAS spectra. All of the values obtained are consistent with the values reported by Bryce[31] and presented in Table 3. The ^{17}O MAS and static NMR spectra of ^{17}O-labeled Ph_3PO were acquired at 9.4 T and are shown in Figure 5. Simulation of the ^{17}O NMR spectra provides the following ^{17}O NMR parameters which are consistent with those of Bryce[31] and which are shown in Table 4: δ_{iso}, the magnitude of $|C_Q|$ and η_Q from MAS spectra, as well as the CS tensor span (Ω), skew (κ), and three Euler angles (α, β, γ) from static spectra.[45] Also, the magnitude of $J_{iso}(^{31}P, ^{17}O)$ obtained from ^{31}P MAS NMR spectra can be confirmed in the ^{17}O MAS spectrum through the measurement of the splittings of each spectral discontinuity. All these NMR parameters for $Ph_3P^{17}O$ were determined to be in

agreement with previously reported values[31] before use in LAG synthesis.

^{31}P SSNMR. ^{31}P CP/MAS SSNMR spectra were recorded at 9.4 T for the ^{17}O-labeled halogen-bonded samples. Spectra were acquired at two different spinning frequencies (ν_{rot} = 3 and 5 kHz) and at two applied magnetic field strengths (4.7 and 9.4 T) to identify the centerband as well as to distinguish the effects of $J_{iso}(^{31}P, ^{17}O)$ from possible impurities. Only the isotropic ^{31}P peaks are shown in Figure 4. The most intense peak in the middle corresponds to those ^{31}P nuclei which are adjacent to zero-spin ^{16}O. The sensitivity of the simulated ^{31}P CP/MAS NMR spectra to the value of $J_{iso}(^{31}P, ^{17}O)$ is demonstrated in Figure S7 (Supporting Information).

Simulations were adjusted by including the effective dipolar coupling constant (R_{eff}) between ^{31}P and ^{17}O, which incorporates the anisotropic part of the J tensor ($R_{eff} = R_{DD} - \Delta J/3$). R_{DD} values were calculated based on the halogen bond geometry from X-ray crystal structures (see Table 1). The R_{eff} values were obtained through iterative spectral fitting. However, the large error in R_{eff} indicates that the R_{eff} values cannot discriminate among the different samples. Therefore, the anisotropy in the J coupling tensor also has low precision. All the ^{31}P CS tensors and J coupling values are summarized in Table 3.

^{17}O-enriched **A2** has a small amount of unknown impurity shown in Figure 4(c) with a pink arrow, which can also be observed also in unlabeled **A2**. However, the poor resolution and low intensity made it impossible measure the value of $J_{iso}(^{31}P, ^{17}O)$.

The $J_{iso}(^{31}P, ^{17}O)$ coupling constants, ranging from 154(4) Hz in compound **A2** to 157(5) Hz in compound **A1**, decrease in the halogen-bonded compounds compared to the starting material ($J_{iso}(^{31}P, ^{17}O)$ = 160(4) Hz). Comparing the two ^{31}P CP/MAS spectra obtained at two different applied magnetic fields can
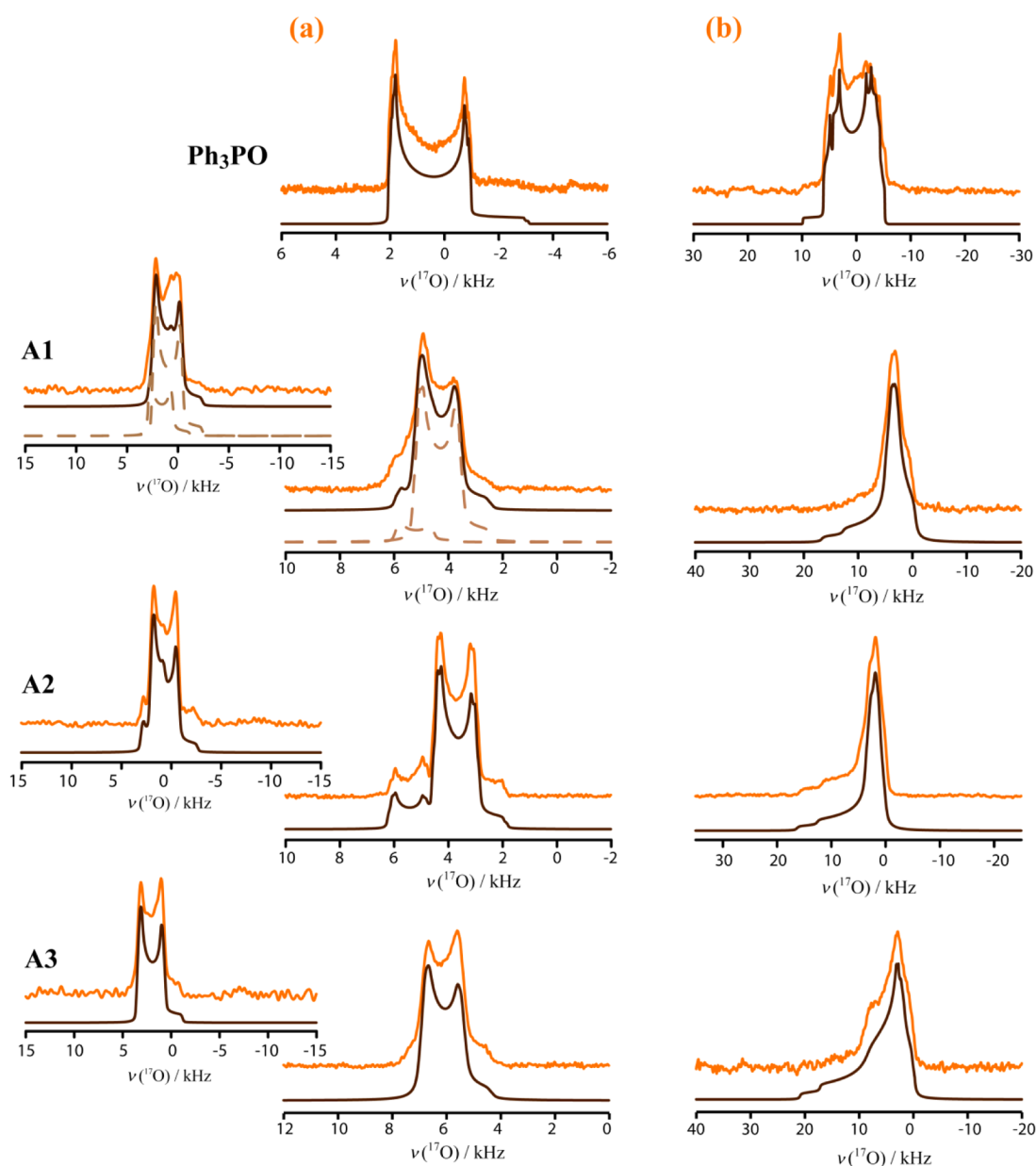
Figure 5. Experimental ^{17}O NMR spectra (orange) of MAS (a) and static (b) Ph$_3$P^{17}O (40%) acquired at 9.4 T and its halogen-bonded compounds (**A1, A2, A3**) acquired at 21.1 T. The corresponding simulated spectra are shown at the bottom (brown). Shown in the insets (left) are the experimental and simulated ^{17}O MAS NMR spectra acquired at 11.7 T. MAS spectra were obtained with spinning speeds of 5.2 kHz at 9.4 T and 10 kHz at 11.7 and 21.1 T.

Table 4. Experimental ^{17}O EFG and CS Tensor Parameters for Ph$_3$PO and Its Halogen-Bonded Compounds[d]

|	δ_{iso}/ppm[a]	Ω/ppm[a]	κ[a]	$|C_Q(^{17}O)|$/ MHz[b]	η_Q[b]	α/°	β/°	γ/°
monoclinic Ph$_3$PO[c]	53.0 (0.2)	155 (5)	−0.75 (0.02)	4.57 (0.01)	0.030 (0.002)	66.5 (3.5)	86.3 (0.5)	8.1 (0.5)
A1	45.6 (0.2)	120 (1)	−0.81 (0.02)	5.03 (0.03)	0.13 (0.01)	78 (1)	81.6 (0.2)	1.9 (0.1)
A2[e]	39.8 (0.2)	121 (1)	−0.89 (0.01)	4.92 (0.01)	0.12 (0.005)	63 (2)	93.4 (0.1)	0.3 (0.2)
A3	59.1 (0.4)	159 (2)	−0.74 (0.01)	4.81 (0.02)	0.13 (0.005)	81 (2)	96.7 (0.2)	11.9 (0.2)

[a]See footnote a in Table 3. [b]The EFG tensor is defined by three principal components V_{11}, V_{22}, and V_{33}, where $|V_{33}| \geq |V_{22}| \geq |V_{11}|$ and $V_{11} + V_{22} + V_{33} = 0$. C_Q is the quadrupolar coupling constant, where $C_Q = ((eQV_{33})/h)$. η_Q is the asymmetry parameter, where $\eta_Q = ((V_{11} - V_{22})/V_{33})$. [c]From ref 31. [d]Error bounds are in brackets. [e]The ^{17}O NMR parameters for the impurity in compound **A2** are δ_{iso} = 53.0(0.4) ppm, $|C_Q(^{17}O)|$ = 4.64(0.06) MHz, and η_Q = 0.10(0.01).

isolate the impurity peak in compound **A1** (shown with pink arrow in Figure 4(b)) from peaks associated with $J_{iso}(^{31}P, ^{17}O)$.

^{17}O SSNMR. Compared to ^{31}P NMR spectroscopy, ^{17}O NMR is expected to provide more straightforward insight into the relationship between NMR properties and halogen bonding

since oxygen is a direct participant in the halogen bond; however, it can be more difficult to acquire and interpret the ^{17}O NMR data because the second-order quadrupolar coupling interaction cannot be averaged under MAS,[46,47] resulting in additional spectral broadening. The ^{17}O MAS NMR spectra for
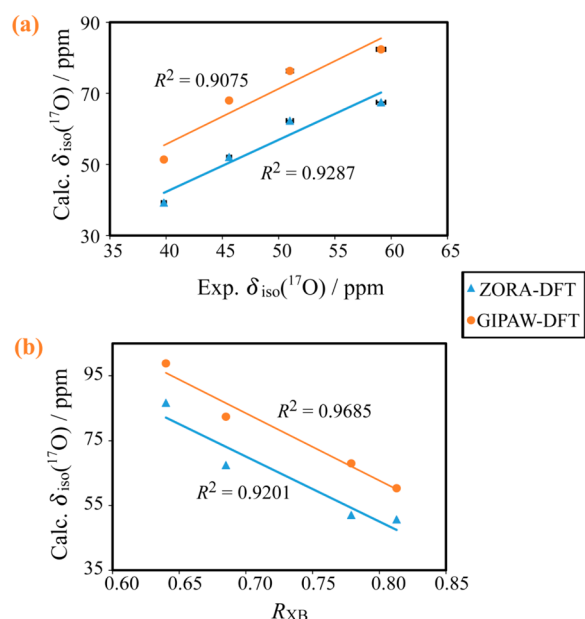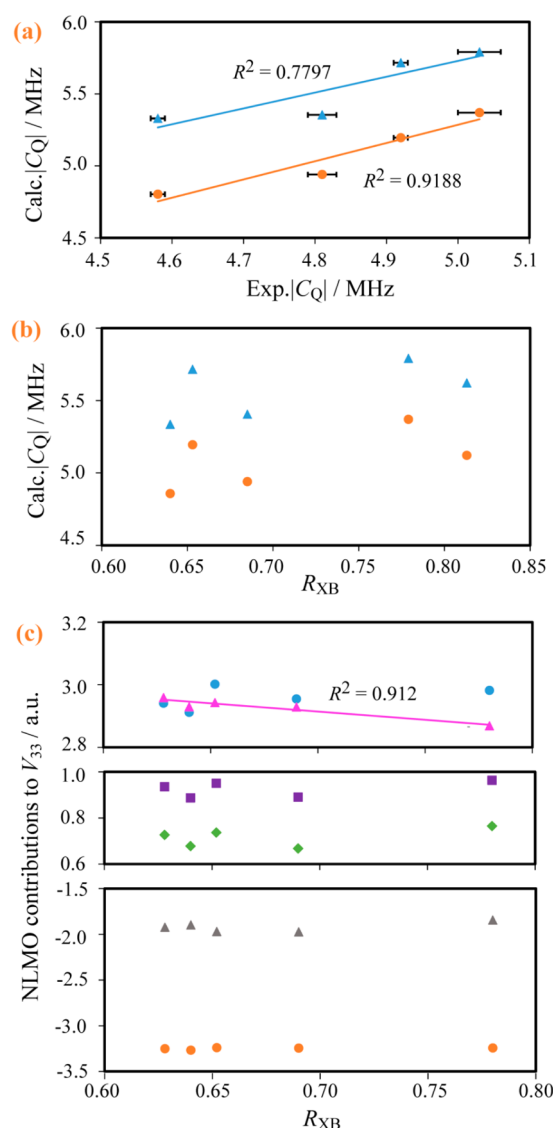
Figure 6. (a) Calculated versus experimental $\delta_{iso}(^{17}O)$ for the ^{17}O-labeled compounds monoclinic Ph_3PO, **A1**, **A2**, and **A3**. (b) A plot of calculated $\delta_{iso}(^{17}O)$ versus R_{XB} values for the halogen-bonded compounds listed in Table 1. Two outliers from **A2** are not plotted in (b). Two different types of DFT calculations were performed: GIPAW DFT calculation using CASTEP (orange circles) and ZORA DFT using ADF (blue triangles). Lines represent the best linear fits: (a) GIPAW: calcd $\delta_{iso}(^{17}O)$ = 1.5609 exp $\delta_{iso}(^{17}O)$ −6.767, ZORA: calcd $\delta_{iso}(^{17}O)$ = 1.4624 exp $\delta_{iso}(^{17}O)$ −16.19; (b) GIPAW: calcd $\delta_{iso}(^{17}O)$ = −207.79R_{XB} + 228.93, ZORA: calcd $\delta_{iso}(^{17}O)$ = −200.33R_{XB} + 210.32.

halogen-bonded compounds were acquired at 21.1 T (shown in Figure 5(a)) and at 11.7 T (shown in the insets) with a spinning rate of 10 kHz. The parameters are summarized in Table 4.

The ^{17}O isotropic chemical shift ranges from 39.8(0.2) ppm for compound **A2** to 59.1(0.4) ppm for compound **A3**. The ^{17}O isotropic chemical shifts for all compounds fall in the known range for phosphine oxides (20−100 ppm).[48] We note that the experimental ^{17}O isotropic chemical shifts in the halogen-bonded compounds do not show a clear trend relative to pure Ph_3PO. Compared to the sometimes substantial effect of *hydrogen* bonding on oxygen chemical shifts, e.g., a change of 29 ppm for the COH groups of α-oxalic acid dihydrate[28] and a change of 125 ppm for carboxyl groups in nucleic acids,[25] the difference caused by halogen bonding in the present study is far less striking.

The magnitude of the quadrupolar coupling constant, $|C_Q(^{17}O)|$, ranges from 4.92(0.01) MHz for compound **A2** to 5.03(0.03) MHz for compound **A1**. The asymmetry parameter, η_Q, is essentially constant at 0.13 for the halogen-bonded compounds. Importantly, however, the value of the ^{17}O quadrupolar coupling constant increases in the presence of the halogen bonding interaction compared with monoclinic ^{17}O-labeled Ph_3PO (see Table 4).

Fitting the ^{17}O MAS NMR spectra obtained at both 11.7 and 21.1 T for compound **A1** allows for the identification of the impurity as the starting material, ^{17}O-labeled Ph_3PO (Figure 5; simulations are shown with brown dashed lines). This is consistent with the small impurity peak found in the ^{31}P CP/MAS NMR spectrum at 4.7 T, whose corresponding chemical shift is 26.3 ppm. It is clear under ^{17}O MAS that compound **A2** contains an unknown <10% impurity (δ_{iso} = 53.0(0.4) ppm,

Figure 7. (a) Calculated versus experimental $|C_Q(^{17}O)|$ values for monoclinic Ph_3PO, **A1**, **A2**, and **A3**. (b) A plot of calculated $|C_Q(^{17}O)|$ values versus R_{XB} values for all of the halogen-bonded compounds listed in Table 1. Two different types of DFT calculation were performed: GIPAW DFT calculation using CASTEP (orange circles) and ZORA DFT using ADF (blue triangles). (c) A plot of the sum of Lewis and non-Lewis largest NLMO contributions to the largest EFG tensor principal component V_{33} as a function of R_{XB} values for the compounds listed in Table 1. Orange circles represent the contribution from the P=O bonding orbital. Blue circles, gray triangles, and pink triangles represent contributions from the oxygen lone pairs along x, y, and z axes, respectively. Green diamonds represent the sum of the four orbitals. Purple squares represent the total contribution. Lines represent the best linear fits: (a) GIPAW: calcd $|C_Q(^{17}O)|$ = 1.2652 exp $|C_Q(^{17}O)|$ − 1.0401; ZORA: calcd $|C_Q(^{17}O)|$ = 1.101 exp $|C_Q(^{17}O)|$ + 0.2242; (c) LP O$_z$: V_{33} = −0.5289R_{XB} + 3.2846.

$|C_Q(^{17}O)|$ = 4.64(0.06) ppm, η_Q = 0.10(0.01)). This can be observed at both 11.7 and 21.1 T.

The ^{17}O static NMR spectra (21.1 T) are shown in Figure 5(b). Simulations of these data provide ^{17}O CS tensors and three Euler angles (α, β, γ), which are summarized in Table 4. However, there is no clear correlation observed between CS tensors or Euler angles and halogen bonding geometry.
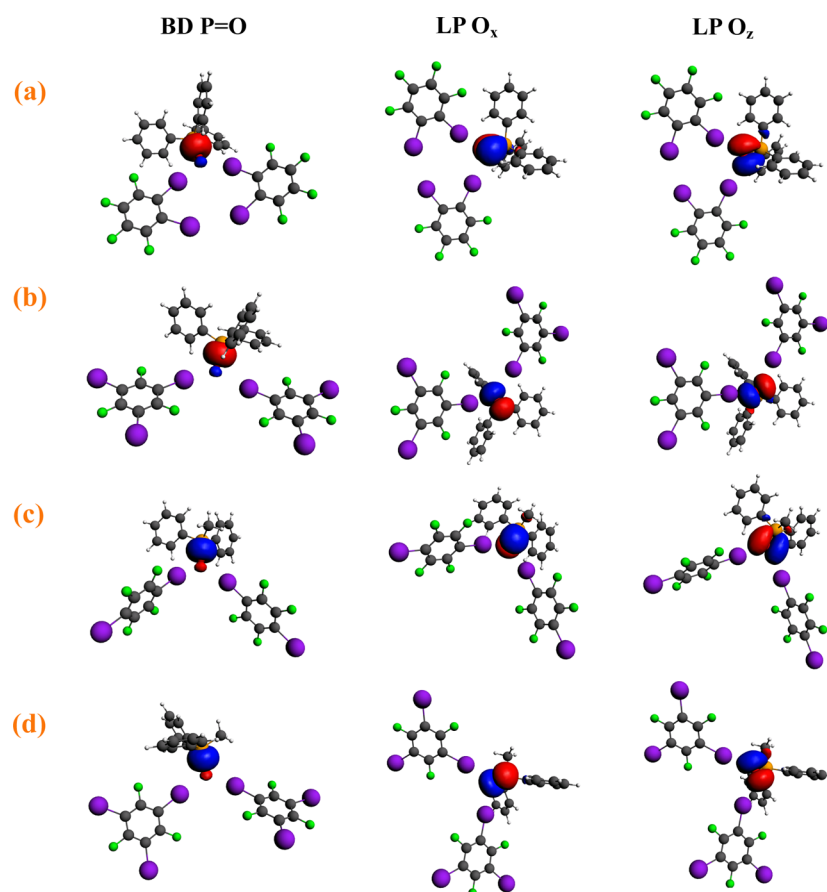
Figure 8. Three major NLMO contributions to ^{17}O EFG tensors for all the halogen-bonded compounds in which oxygen acts as a bifurcated halogen bond acceptor (**A2** (a), **A3** (b), **B1** (c), and **B3** (d)). The main NLMO contributions are from the bonding orbitals between P and O (BD P=O), the O lone pair along the x axis (LP O_x), and the O lone pair along the z axis (LP O_z).

Computational Analysis. *(i). Calculated Chemical Shifts and the Halogen Bond Geometry.* Calculations of ^{31}P and ^{17}O magnetic shielding tensors were carried out using either GIPAW DFT with the PBE functional in CASTEP or ZORA DFT with the revPBE functional implemented in ADF. In Figure 6(a), the calculated ^{17}O isotropic chemical shifts are plotted versus the experimental values. The calculated isotropic chemical shifts from GIPAW DFT more strongly overestimate the experimental data than do the values obtained from ZORA DFT. This overestimation might result from a lack of inclusion of relativistic effects associated with the iodine involved in halogen bonding.[49] However, the trend in $\delta_{iso}(^{17}O)$ is well-reproduced by both sets of calculations, with correlation coefficients, R^2, of 0.9075 and 0.9287, respectively. Figure 6(b) shows an inverse linear correlation between the R_{XB} values and calculated $\delta_{iso}(^{17}O)$ values for both sets of calculations ($R^2 = 0.9685$ for GIPAW; $R^2 = 0.9201$ for ZORA). For those cocrystals with more than one iodine halogen bond donor to each oxygen site, a cumulative R_{XB} value was used (i.e., $R_{XB} = 1 - (1 - R_{XB}$ (donor1)$) - (1 - R_{XB}$ (donor2)$) - ...$).[17] Two outlier points for **A2** are excluded from the linear fit in Figure 6(b). Since the calculated $\delta_{iso}(^{17}O)$ for **A2** are in good agreement with the experimental values, it is not immediately clear why they are outliers in the second plot. Compared to the other compounds, an additional iodine atom in o-$C_6F_4I_2$ is close to the oxygen atom. Perhaps extra relativistic and/or XB effects from the nearby heavy iodine atom may lead to further chemical shift changes in compound **A2**.
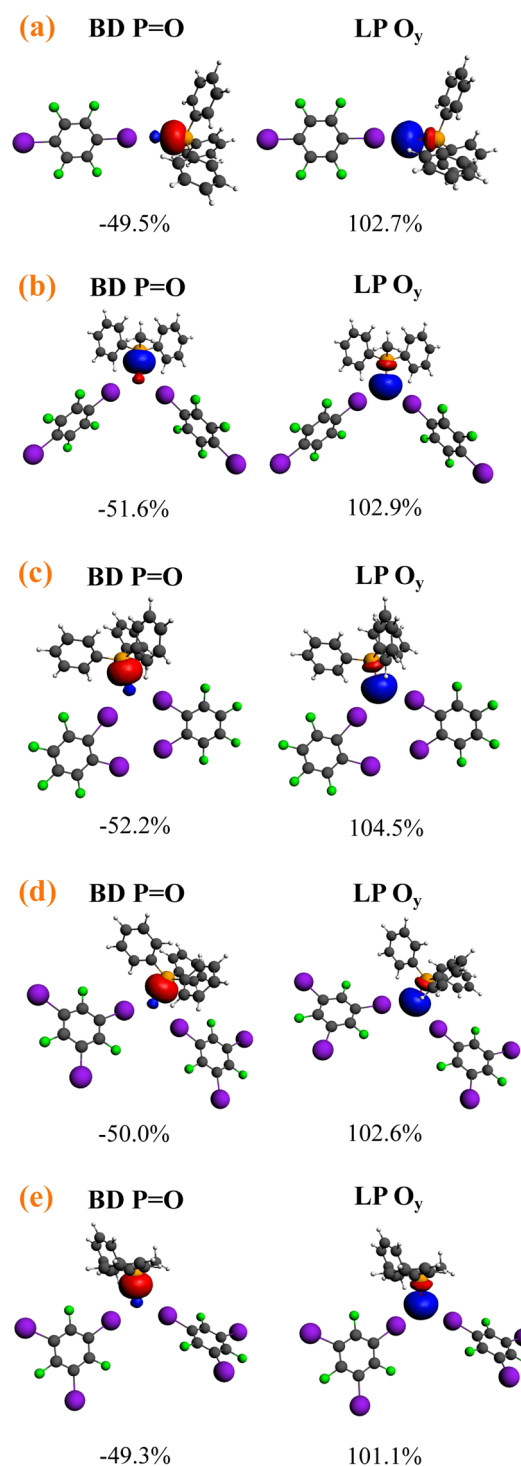
There is no clear correlation between calculated $\delta_{iso}(^{31}P)$ and R_{XB} values or P=O bond distance that could be distinguished for the halogen-bonded compounds (see Figure S8(b) and (c)). There are two factors which explain the poor correlation. First, the phosphorus is indirectly involved in halogen bonding interaction. The effect of the iodine−oxygen halogen bond on the ^{31}P NMR parameters might not be the major contribution. Second, Alvarado and co-workers found that phosphine−chalcogen bond angles and geometry heavily impact ^{31}P chemical shifts, leading to a poor correlation between ^{31}P chemical shifts and phosphine−chalcogen bond energy.[50] In our case, the presence of halogen bonding results in widely variable P=O⋯I angles, ranging from 116.4° to 152.1° (see in Table 1). This variability likely also contributes to the ^{31}P chemical shifts.

(ii). Analysis of Calculated Oxygen Quadrupolar Coupling Tensors. Halogen Bond Geometry and NLMO Contributions. A plot of experimental vs calculated ^{17}O quadrupolar coupling constants for Ph_3PO, **A1**, **A2**, and **A3** is presented in Figure 7(a). PAW DFT provides a better correlation ($R^2 = 0.9188$) relative to a calculation done using a cluster model in ADF ($R^2 = 0.7797$). The weaker correlation could be due to the neglect of the full crystal lattice. Shown in Figure 7(b) is a plot of the calculated $|C_Q(^{17}O)|$ values versus the cumulative R_{XB} value determined from X-ray crystallography for all of the halogen-bonded compounds. While the calculated $|C_Q(^{17}O)|$ tends to increase as the halogen bonding weakens, there is a significant degree of scatter in these data.
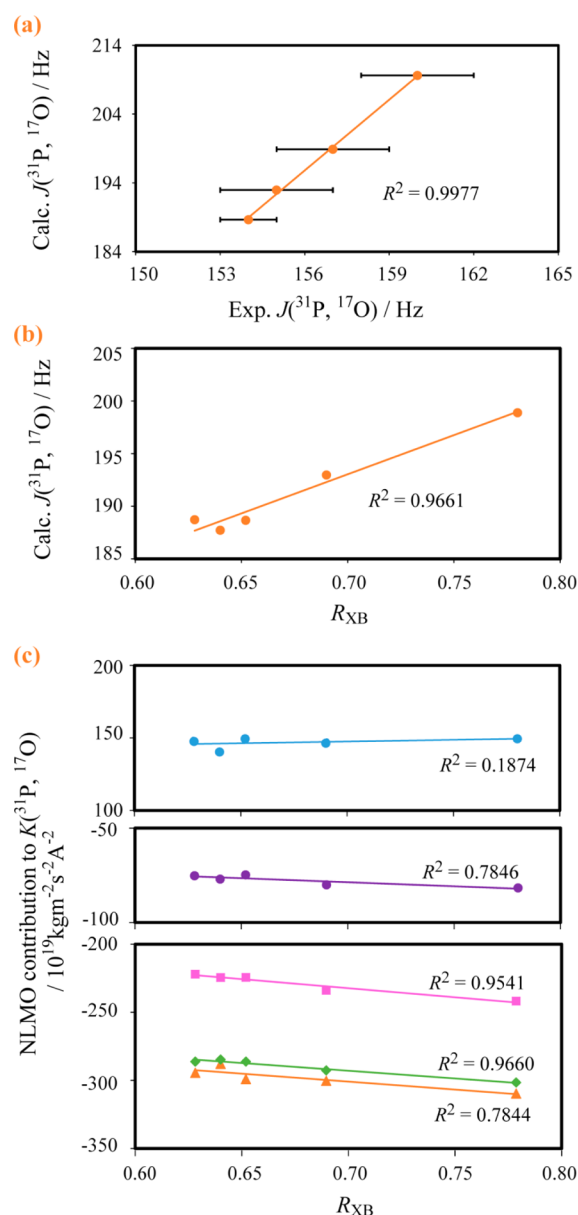
Figure 9. (a) Calculated versus experimental $J(^{31}P, {}^{17}O)$ values for monoclinic Ph$_3$PO, **A1**, **A2**, and **A3**. (b) Plot of calculated $J(^{31}P, {}^{17}O)$ values versus R_{XB} values for the compounds listed in Table 1. (c) A plot of the sum of Lewis and non-Lewis largest NLMO contributions to $J(^{31}P, {}^{17}O)$ as a function of R_{XB} values for **A1**, **A2**, **A3**, **B1**, and **B3**. Blue circles represent the contribution from the P=O bonding orbital (BD P=O). Orange triangles represent the contribution from the oxygen lone pair (LP O$_y$). Purple circles represent the contribution from the oxygen core orbital (CR O), and pink squares represent the sum of the three major contributions (the oxygen lone pair orbital, the oxygen core orbitals, and the P=O bonding orbitals). Green diamonds represent the total contribution. Lines represent the best linear fits: (a) calcd $J(^{31}P, {}^{17}O) = 3.4296$ exp. $J(^{31}P, {}^{17}O) - 339.2$; (b) calcd $J(^{31}P, {}^{17}O) = 74.375R_{XB} + 140.97$; (c) BD P=O: $K = 26.487R_{XB} + 128.68$; LP O$_y$: $K = -115.54R_{XB} - 219.95$; CR O: $K = -43.081R_{XB} - 48.541$; sum of three orbitals: $K = -132.14R_{XB} - 139.8$; total: $K = -112.23R_{XB} - 214.25$.

Figure 10. Two major NLMO contributions to the isotropic $J(^{31}P, {}^{17}O)$ coupling values for all the halogen-bonded compounds (**A1** (a), **B1** (b), **A2** (c), **A3** (d), and **B3** (e)). The main NLMO contributions are from the bonding orbitals between P and O (BD P=O) and the O lone pair along the y axis (LP O$_y$).

A further NLMO analysis elucidates the connection between the ^{17}O EFG tensor and the electronic structure of the halogen bond (see Table S4 in the Supporting Information). Since the largest principal component, V_{33}, determines the value of $C_Q(^{17}O)$, the NLMO analysis is conducted on V_{33} for all

halogen-bonded compounds. As shown in Figures 7 and 8 (see also the Supporting Information), four key molecular orbitals contribute to the value of V_{33}: the bonding orbital between phosphorus and oxygen and three different oxygen lone pair orbitals. If we treat the P=O bond as the y axis, the first oxygen lone pair orbital (LP O$_x$) is always along the x axis, which is perpendicular to the phenyl ring in Ph$_3$PO or methyl group in

CH_3Ph_2PO, whereas the second oxygen lone pair orbital (LP O_z) is always aligned with the z axis. The oxygen lone pair orbital (LP O_y) which is aligned with the P=O bond makes a negative contribution to oxygen EFG tensors.

Each major NLMO contribution related to halogen bonding is plotted as a function of the R_{XB} value (Figure 7(c)). It is noted that most of the major NLMO contributions, i.e., the bonding orbitals between P and O and the oxygen lone pair orbital along the x and y axes, are not well-correlated with the R_{XB} values. This corroborates the lack of a clear correlation between oxygen quadrupolar coupling and R_{XB} values (Figure 7(b)). However, it is clear that the contribution from the oxygen lone pair orbital along the z axis, the p_z-type orbital,[51] correlates in a linear fashion ($R^2 = 0.91$) with R_{XB}. Since the lobes of this oxygen lone pair are oriented toward the iodine atom, especially when oxygen acts as a bifurcated halogen bond acceptor (see LP O_z in Figure 8), the contribution from this orbital correlates strongly to the halogen bond. Finally, the contribution from the P=O bonding orbital reduces the overall value of V_{33}. As the halogen bonding interaction weakens, the contribution from the P=O bonding orbital decreases.

(iii). Analysis of Computed J(^{31}P, ^{17}O) Values. A plot of the calculated $J(^{31}P, ^{17}O)$ coupling constants versus the experimental values for ^{17}O-labeled Ph$_3$PO and its related halogen-bonded cocrystals (**A1**, **A2**, **A3**) is provided in Figure 9(a). Even though the calculated $J(^{31}P, ^{17}O)$ values are overestimated, they are still well-reproduced ($R^2 = 0.9977$).

A plot of calculated $J(^{31}P, ^{17}O)$ coupling constants versus R_{XB} shows a strong positive correlation (Figure 9(b)). The $J(^{31}P, ^{17}O)$ coupling constant increases as the halogen bonding interaction weakens, which is consistent with what we have previously reported for $J(^{31}P, ^{77}Se)$ coupling constants in halogen-bonded phosphine selenides.[17] In order to probe the origins of the $J(^{31}P, ^{17}O)$ coupling constant, we performed an NLMO analysis to determine the major molecular orbital contributions (see Table S3 in the Supporting Information). The three main NLMO contributions are the bonding P=O orbital, one O lone pair orbital along the P=O bond axis, and one O core orbital. The results are shown in Figure 10 and in the Supporting Information. The key contribution to the $J(^{31}P, ^{17}O)$ coupling constant is from the oxygen lone pair orbital, and the second contribution is from the bonding P=O orbitals and oxygen core orbital. Unlike the NLMO contributions to the ^{17}O EFG tensors, the oxygen lone pair orbital aligned with the P=O bond, which is the p_y orbital, makes a large positive contribution to $J(^{31}P, ^{17}O)$. The percentages shown in Figure 10 represent how much each molecular orbital contributes to the calculated $J(^{31}P, ^{17}O)$ coupling constant. A negative contribution to calculated $J(^{31}P, ^{17}O)$ values arises from the P=O bonding orbitals, opposite in sign to the total NLMO contribution value. The presence of halogen bonding will lengthen the P=O bond and thus reduce the $J(^{31}P, ^{17}O)$ coupling constant. A plot of each major contribution, the sum of the three major contributions, and the total values including all minor contributions as a function of R_{XB} values are presented in Figure 9(c). It can be seen how the sum of the three main contributions and the total contributions follow the same trend relative to the R_{XB} values. Only the oxygen lone pair and core orbitals closely follow the overall linear trend. However, there is no real correlation between the contribution from the P=O bonding orbital and the R_{XB} values ($R^2 = 0.1874$).

CONCLUSIONS

A series of halogen-bonded compounds containing P=O···I−C motifs has been prepared by simple mechanochemical liquid-assisted grinding. Nonlabeled and ^{17}O-labeled compounds have been characterized by single-crystal X-ray diffraction and ^{31}P and ^{17}O solid-state NMR. Using atomic coordinates extracted from the crystal structures, two types of density functional theory computations have been applied to interpret the correlation between the halogen bonding strength, quantified by R_{XB}, and the NMR parameters (^{31}P and ^{17}O chemical shifts, ^{17}O quadrupolar coupling constants, and $J(^{31}P, ^{17}O)$ coupling constants).

The following main conclusions may be drawn from these studies:

(1) From the ^{31}P CP/MAS NMR spectra, the complete ^{31}P chemical shift tensors have been measured. We observe a small increase in the ^{31}P chemical shift and a small decrease in the span in the halogen-bonded compounds relative to the pure starting materials. Therefore, the ^{31}P CS tensors can be an indirect indication of the presence of halogen bonding interaction.

(2) ^{31}P solid-state NMR spectra of ^{17}O-labeled halogen-bonded compounds reveal an increase in the value of the $J(^{31}P, ^{17}O)$ coupling constant when the P=O···I−C halogen bond weakens.

(3) A direct ^{17}O solid-state NMR study of the halogen bonding acceptor provides several correlations between the NMR parameters and halogen bonding strength. The measurement of ^{17}O EFG tensors shows that both the ^{17}O quadrupolar coupling constant and asymmetry parameter increase in the presence of a halogen bonding interaction. However, there is no clear relationship noted between the experimental ^{17}O isotropic chemical shift and halogen bonding.

(4) DFT calculations of the NMR parameters reveal several remarkable trends. The GIPAW DFT calculations, which take the full crystal packing into account, are in good agreement with experiment. The calculations also indicate correlations between the ^{17}O isotropic chemical shift as well as $J(^{31}P, ^{17}O)$ coupling and halogen bonding strength.

(5) A natural localized molecular orbital analysis provided insight into the orbital contributions to the $J(^{31}P, ^{17}O)$ coupling constants and the ^{17}O EFG tensors in the P=O···I−C motif. The values of $J(^{31}P, ^{17}O)$ arise mainly due to contributions from the bonding orbital between phosphorus and oxygen, the oxygen lone pair aligned with the P=O bond, and the oxygen core orbital. The key contributions to the ^{17}O quadrupolar coupling constant are due to the bonding orbital between phosphorus and oxygen and the oxygen lone pair orbitals. The contribution from the oxygen p_z orbital has a linear correlation with the strength of the halogen bonding interaction.

Overall, this first study of ^{17}O NMR parameters in halogen-bonded solids has provided key experimental and computational insights into the relationship between NMR observables and the nature of the halogen bond.

ASSOCIATED CONTENT

ⓈSupporting Information

The Supporting Information is available free of charge on the ACS Publications website at DOI: 10.1021/acs.jpcc.5b09737.

Additional diffractograms, spectra, computational results, and information on single-crystal structure refinements (PDF)

Crystallographic information for C30 H15 F8 I4 O P (CIF)

Crystallographic information for C24 H15 F3 I3 O P (CIF)

Crystallographic information for C21 H16 F4 I2 N O P (CIF)

Crystallographic information for C30 H15 F8 I4 O P (CIF)

Crystallographic information for C25 H13 F6 I6 O P (CIF)

■ AUTHOR INFORMATION

Corresponding Author

*Tel.: +1-613-562-5800 ext. 2018. Fax: +613-562-5170. E-mail: dbryce@uottawa.ca.

Notes

The authors declare no competing financial interest.

■ REFERENCES

(1) Clark, T.; Hennemann, M.; Murray, J. S.; Politzer, P. Halogen Bonding: The σ-Hole. *J. Mol. Model.* **2007**, *13*, 291−296.

(2) Desiraju, G. R.; Ho, P. S.; Kloo, L.; Legon, A. C.; Marquardt, R.; Metrangolo, P.; Politzer, P.; Resnati, G.; Rissanen, K. Definition of the Halogen Bond (IUPAC Recommendations 2013). *Pure Appl. Chem.* **2013**, *85*, 1711−1713.

(3) Cavallo, G.; Metrangolo, P.; Pilati, T.; Resnati, G.; Terraneo, G. Naming Interactions from the Electrophilic Site. *Cryst. Growth Des.* **2014**, *14*, 2697−2702.

(4) Gilday, L. C.; Robinson, S. W.; Barendt, T. A.; Langton, M. J.; Mullaney, B. R.; Beer, P. D. Halogen Bonding in Supramolecular Chemistry. *Chem. Rev.* **2015**, *115*, 7118−7195.

(5) Metrangolo, P.; Meyer, F.; Pilati, T.; Resnati, G.; Terraneo, G. Halogen Bonding in Supramolecular Chemistry. *Angew. Chem., Int. Ed.* **2008**, *47*, 6114−6127.

(6) Voth, A. R.; Hays, F. A.; Ho, P. S. Directing Macromolecular Conformation Through Halogen Bonds. *Proc. Natl. Acad. Sci. U. S. A.* **2007**, *104*, 6188−6193.

(7) Bolton, O.; Lee, K.; Kim, H.-J.; Lin, K. Y.; Kim, J. Activating Efficient Phosphorescence From Purely Organic Materials by Crystal Design. *Nat. Chem.* **2011**, *3*, 205−210.

(8) Jungbauer, S. H.; Walter, S. M.; Schindler, S.; Rout, L.; Kniep, F.; Huber, S. M. Activation of a Carbonyl Compound by Halogen Bonding. *Chem. Commun.* **2014**, *50*, 6281−6284.

(9) Himmel, D. M.; Das, K.; Clark, A. D.; Hughes, S. H.; Benjahad, A.; Oumouch, S.; Guillemont, J.; Coupa, S.; Poncelet, A.; Csoka, I.; et al. Crystal Structures for HIV-1 Reverse Transcriptase in Complexes with Three Pyridinone Derivatives: A New Class of Non-Nucleoside Inhibitors Effective against a Broad Range of Drug-Resistant Strains. *J. Med. Chem.* **2005**, *48*, 7582−7591.

(10) Thorson, R. A.; Woller, G. R.; Driscoll, Z. L.; Geiger, B. E.; Moss, C. A.; Schlapper, A. L.; Speetzen, E. D.; Bosch, E.; Erdélyi, M.; Bowling, N. P. Intramolecular Halogen Bonding in Solution: ^{15}N, ^{13}C, and ^{19}F NMR Studies of Temperature and Solvent Effects. *Eur. J. Org. Chem.* **2015**, *2015*, 1685−1695.

(11) Ciancaleoni, G.; Bertani, R.; Rocchigiani, L.; Sgarbossa, P.; Zuccaccia, C.; Macchioni, A. Discriminating Halogen-Bonding from Other Noncovalent Interactions by a Combined NOE NMR/DFT Approach. *Chem. - Eur. J.* **2015**, *21*, 440−447.

(12) Weingarth, M.; Raouafi, N.; Jouvelet, B.; Duma, L.; Bodenhausen, G.; Boujlel, K.; Schöllhorn, B.; Tekely, P. Revealing Molecular Self-Assembly and Geometry of Non-Covalent Halogen Bonding by Solid-State NMR Spectroscopy. *Chem. Commun.* **2008**, 5981−5983.

(13) Bryce, D. L.; Viger-Gravel, J. Solid-State NMR Study of Halogen-Bonded Adducts, in *Halogen Bonding I*; Metrangolo, P., Resnati, G., Eds.; Springer: Heidelberg, 2015; pp 183−203.

(14) Attrell, R. J.; Widdifield, C. M.; Korobkov, I.; Bryce, D. L. Weak Halogen Bonding in Solid Haloanilinium Halides Probed Directly via Chlorine-35, Bromine-81, and Iodine-127 NMR Spectroscopy. *Cryst. Growth Des.* **2012**, *12*, 1641−1653.

(15) Viger-Gravel, J.; Leclerc, S.; Korobkov, I.; Bryce, D. L. Correlation Between ^{13}C Chemical Shifts and the Halogen Bonding Environment in a Series of Solid para-Diiodotetrafluorobenzene Complexes. *CrystEngComm* **2013**, *15*, 3168−3177.

(16) Viger-Gravel, J.; Leclerc, S.; Korobkov, I.; Bryce, D. L. Direct Investigation of Halogen Bonds by Solid-State Multinuclear Magnetic Resonance Spectroscopy and Molecular Orbital Analysis. *J. Am. Chem. Soc.* **2014**, *136*, 6929−6942.

(17) Viger-Gravel, J.; Meyer, J. E.; Korobkov, I.; Bryce, D. L. Probing Halogen Bonds With Solid-State NMR Spectroscopy: Observation and Interpretation of J(^{77}Se,^{31}P) Coupling in Halogen-Bonded P═Se···I Motifs. *CrystEngComm* **2014**, *16*, 7285−7297.

(18) Mechanochemistry: From Functional Solids to Single Molecules. *Faraday Discuss.* **2014**, *170*, 1−432.10.1039/C4FD90051K

(19) Shan, N.; Toda, F.; Jones, W. Mechanochemistry and Co-Crystal Formation: Effect of Solvent on Reaction Kinetics. *Chem. Commun.* **2002**, 2372−2373.

(20) Fernandes, J. A.; Sardo, M.; Mafra, L.; Choquesillo-Lazarte, D.; Masciocchi, N. X-ray and NMR Crystallography Studies of Novel Theophylline Cocrystals Prepared by Liquid Assisted Grinding. *Cryst. Growth Des.* **2015**, *15*, 3674−3683.

(21) Oh, S. Y.; Nickels, C. W.; Garcia, F.; Jones, W.; Friščić, T. Switching Between Halogen- and Hydrogen-Bonding in Stoichiometric Variations of a Cocrystal of a Phosphine Oxide. *CrystEngComm* **2012**, *14*, 6110−6114.

(22) Bowmaker, G. A.; Hanna, J. V.; Hart, R. D.; Healy, P. C.; King, S. P.; Marchetti, F.; Pettinari, C.; Skelton, B. W.; Tabacaru, A.; White, A. H. Mechanochemical and Solution Synthesis, X-ray Structure and IR and ^{31}P Solid State NMR Spectroscopic Studies of Copper(I) Thiocyanate Adducts with Bulky Monodentate Tertiary Phosphine Ligands. *Dalton Trans.* **2012**, *41*, 7513−7525.

(23) Gerothanassis, I. P. Oxygen-17 NMR. In *Encyclopedia of Nuclear Magnetic Resonance*; Grant, D. M., Harris, R. K., Eds.; John Wiley & Sons: Chichester, U. K., 1996; pp 3430−3438.

(24) Wu, G.; Mason, P.; Mo, X.; Terskikh, V. Experimental and Computational Characterization of the ^{17}O Quadrupole Coupling and Magnetic Shielding Tensors for p-Nitrobenzaldehyde and Form-aldehyde. *J. Phys. Chem. A* **2008**, *112*, 1024−1032.

(25) Wu, G.; Dong, S.; Ida, R.; Reen, N. A Solid-State ^{17}O Nuclear Magnetic Resonance Study of Nucleic Acid Bases. *J. Am. Chem. Soc.* **2002**, *124*, 1768−1777.

(26) Wang, W. D.; Lucier, B. E. G.; Terskikh, V. V.; Wang, W.; Huang, Y. Wobbling and Hopping: Studying Dynamics of CO_2 Adsorbed in Metal−Organic Frameworks via ^{17}O Solid-State NMR. *J. Phys. Chem. Lett.* **2014**, *5*, 3360−3365.

(27) Vogt, F. G.; Yin, H.; Forcino, R. G.; Wu, L. ^{17}O Solid-State NMR as a Sensitive Probe of Hydrogen Bonding in Crystalline and Amorphous Solid Forms of Diflunisal. *Mol. Pharmaceutics* **2013**, *10*, 3433−3446.

(28) Zhang, Q.-W.; Chekmenev, E. Y.; Wittebort, R. J. ^{17}O Quadrupole Coupling and Chemical Shielding Tensors in an H-bonded Carboxyl Group: α-Oxalic Acid. *J. Am. Chem. Soc.* **2003**, *125*, 9140−9146.

(29) Cinčić, D.; Friščić, T.; Jones, W. Experimental and Database Studies of Three-Centered Halogen Bonds with Bifurcated Acceptors Present in Molecular Crystals, Cocrystals and Salts. *CrystEngComm* **2011**, *13*, 3224−3231.

(30) Friščić, T.; Trask, A. V.; Jones, W.; Motherwell, W. D. S. Screening for Inclusion Compounds and Systematic Construction of Three-Component Solids by Liquid-Assisted Grinding. *Angew. Chem., Int. Ed.* **2006**, *45*, 7546−7550.

(31) Bryce, D. L.; Eichele, K.; Wasylishen, R. E. An ^{17}O NMR and Quantum Chemical Study of Monoclinic and Orthorhombic Polymorphs of Triphenylphosphine Oxide. *Inorg. Chem.* **2003**, *42*, 5085−5096.

(32) *APEX Software Suite*; Bruker AXS Inc.: Madison, WI, 2012.

(33) *SADABS*; Bruker AXS Inc.: Madison, WI, 2001.

(34) Sheldrick, G. M. Crystal Structure Refinement with SHELXL. *Acta Crystallogr., Sect. C: Struct. Chem.* **2015**, *71*, 3−8.

(35) Eichele, K. *Herzfeld-Berger analysis program*, version 1.7.5.; Universität Tübingen: Tübingen, Germany, 2015.

(36) Eichele, K. *WSolids1*, version 1.20.21.; Universität Tübingen: Tübingen, Germany, 2013.

(37) Clark, S. J.; Segall, M. D.; Pickard, C. J.; Hasnip, P. J.; Probert, M. I. J.; Refson, K.; Payne, M. C. First Principles Methods Using CASTEP. *Z. Kristallogr. - Cryst. Mater.* **2005**, *220*, 567−570.

(38) Baerends, E. J.; et al. Amsterdam Density Functional Software, ADF2012.01 SCM; *Theoretical Chemistry*; Vrije Universiteit: Amsterdam, The Netherlands, 2012.

(39) Pickard, C. J.; Mauri, F. All-Electron Magnetic Response with Pseudopotentials: NMR Chemical Shifts. *Phys. Rev. B: Condens. Matter Mater. Phys.* **2001**, *63*, 245101.

(40) Frisch, M. J.; et al. *Gaussian 09*, Revision A.02; Gaussian Inc.: Wallingford, CT, 2009.

(41) Jameson, C. J.; De Dios, A.; Jameson, A. K. Absolute Shielding Scale for ^{31}P From Gas-Phase NMR Studies. *Chem. Phys. Lett.* **1990**, *167*, 575−582.

(42) Wasylishen, R. E.; Bryce, D. L. A Revised Experimental Absolute Magnetic Shielding Scale for Oxygen. *J. Chem. Phys.* **2002**, *117*, 10061−10066.

(43) Bondi, A. van der Waals Volumes and Radii. *J. Phys. Chem.* **1964**, *68*, 441−451.

(44) Arumugam, S.; Glidewell, C.; Harris, K. D. M. Probing Hydrogen-Bonding Patterns in Cocrystals of Amides and Triarylphosphine Oxides Using High-Resolution Solid-State ^{31}P NMR Spectroscopy. *J. Chem. Soc., Chem. Commun.* **1992**, 724−726.

(45) Bryce, D. L. Tensor Interplay. In *NMR Crystallography*; Harris, R. K., Wasylishen, R. E., Duer, M. J., Eds.; John Wiley and Sons Ltd.: Chichester, U. K., 2009; pp 289−301.

(46) Bryce, D. L.; Bernard, G. M.; Gee, M.; Lumsden, M. D.; Eichele, K.; Wasylishen, R. E. Practical Aspects of Modern Routine Solid-State Multinuclear Magnetic Resonance Spectroscopy: One-Dimensional Experiments. *Can. J. Anal. Sci. Spectrosc.* **2001**, *46*, 46−82.

(47) Kentgens, A. P. M. A Practical Guide to Solid-State NMR of Half-Integer Quadrupolar Nuclei With Some Applications to Disordered Systems. *Geoderma* **1997**, *80*, 271−306.

(48) Berger, S.; Braun, S.; Kalinowski, H.-O. *NMR Spectroscopy of the Non-Metallic Elements*; Becconsali, J., English language translation; John Wiley & Sons: Chichester, U. K., 1997; Chapter 5.

(49) Kutzelnigg, W. Fundamentals of Nonrelativistic and Relativistic Theory of NMR and EPR Parameters. In *Calculation of NMR and EPR Parameters: Theory and Applications*; Kaupp, M., Bühl, M., Malkin, V. G., Eds.; Wiley-VCH: Weinheim, 2004; pp 43−82.

(50) Alvarado, S. R.; Shortt, I. A.; Fan, H.-J.; Vela, J. Assessing Phosphine−Chalcogen Bond Energetics from Calculations. *Organometallics* **2015**, *34*, 4023−4031.

(51) Autschbach, J.; Zheng, S.-H.; Schurko, R. W. Analysis of Electric Field Gradient Tensors at Quadrupolar Nuclei in Common Structural Motifs. *Concepts Magn. Reson., Part A* **2010**, *36A*, 84−126.